

Printed thermoelectric materials and devices: Fabrication techniques, advantages, and challenges

Michael Orrill, Saniya LeBlanc

Mechanical and Aerospace Engineering Department, The George Washington University,
 Washington District of Columbia 20052

Correspondence to: S. LeBlanc (E-mail: sleblanc@email.gwu.edu)

ABSTRACT: Thermoelectric (TE) devices enable increased efficiency and performance by converting waste heat to usable electricity or providing solid-state, localized cooling. Large-scale implementation of the technology is hindered by power conversion efficiency, manufacturing challenges, and material and system costs. Traditionally, inorganic compounds like bismuth telluride and lead telluride are used for their high performance, but they are brittle, scarce, and toxic. Organic compounds have lower power conversion efficiencies, but they are flexible, abundant, low-cost, environmentally benign, and solution-processable, making them suitable for large-scale, high-throughput manufacturing techniques such as roll-to-roll printing. Inorganic–organic hybrid composite materials can boost power conversions efficiencies while maintaining ease of processing. This review summarizes and compares four manufacturing techniques—inkjet, screen, and dispenser printing, and stereolithography—used to fabricate TE devices. Common challenges relevant to printed TE materials and devices are described, and recent research results using these techniques are also reviewed. © 2016 Wiley Periodicals, Inc. *J. Appl. Polym. Sci.* **2016**, *133*, 44256.

KEYWORDS: composites; conducting polymers; manufacturing; nanoparticles; nanowires and nanocrystals; thermal properties

Received 28 March 2016; accepted 1 August 2016

DOI: 10.1002/app.44256

INTRODUCTION

Thermoelectric (TE) devices are solid-state devices that generate electrical power or pump heat. They are particularly interesting for power generation because they can convert waste heat directly into electricity. Almost 60% of energy resources consumed in the US are rejected in the form of heat, so waste heat recovery using TE generators would enable valuable improvements in energy efficiency.^{1,2} The TE figure of merit is given by $ZT = S^2\sigma T/\kappa$ where S is the Seebeck coefficient, σ and κ are the electrical and thermal conductivities, respectively, and T is the absolute temperature. Two relationships between these properties limit improvement in ZT . First, the Seebeck coefficient and electrical conductivity are inversely related, and second, the electron contribution to thermal conductivity, described by the Wiedemann–Franz Law, is directly proportional to electrical conductivity. The desire to use energy resources more efficiently has led to growth in the research and development of TE materials and devices. Notably, polymer-based TE materials could enable low-temperature waste heat recovery with flexible,³ inexpensive devices. Polymer TE devices are often fabricated via printing methods, and the manufacturing method can influence the device development and performance. This review discusses

printing fabrication techniques as applied to polymer-based TE materials and devices.

The most commonly studied TE materials are semimetals and doped semiconductors.⁴ State-of-the-art TE materials are variations of chalcogenides, silicides, clathrates, skutterudites, half-Heusler alloys, and oxides,⁵ with promising developments related to tetrahedrites presented in recent years. Commercial TE devices based on bismuth telluride are widely available and used predominantly for localized heating/cooling applications. Commercial TE devices for large-scale waste heat recovery have become available very recently, and prototypes and feasibility studies have been reported for industrial processes.⁶ Scarcity, toxicity, the high costs of raw materials, and processing of the composing elements, including Bi, Te, Sb, and Pb, are obstacles to widespread commercialization of TE devices,⁴ and the manufacturing and system-level costs of commercial devices are significant components of overall device cost.^{5,7} The heavy and brittle nature of inorganic TE materials also limits feasibility in many waste heat recovery applications involving transportation and non-planar surfaces since high specific power and flexibility/conformability are desirable.

Michael Dustin Orrill is a PhD student at The George Washington University's Department of Mechanical and Aerospace Engineering. He graduated magna cum laude with a Bachelors of Science in Mechanical Engineering at Northern Arizona University in 2014. He also earned an Associate of Arts degree in Psychology from Coconino Community College in 2010. His research interests are found in materials science and nanotechnology for sustainable energy technologies.



Dr. Saniya LeBlanc is an assistant professor in the Department of Mechanical and Aerospace Engineering at The George Washington University. She uses scalable manufacturing techniques to create materials for energy applications. Previously, she was at Alphabet Energy where she created research, development, and manufacturing solutions for thermoelectric technologies and evaluated new power generation materials. Dr. LeBlanc obtained an MS and PhD in mechanical engineering at Stanford University and a BS from Georgia Institute of Technology.



Organic materials are low cost, low density, mechanically flexible, non-toxic, solution-processable, and have very low intrinsic thermal conductivities.⁸ The electronic structure of conductive and semiconducting organic materials is fairly tunable via chemical or electrochemical doping treatments.⁹ Early research on organic TE materials focused on conjugated polymers including polyaniline, polypyrrole, and polythiophene, but these polymers suffer from relatively low electrical conductivity. Poly(3,4-ethylenedioxy-thiophene) (PEDOT), most often paired with poly(styrenesulfonate) (PEDOT:PSS), has high electrical conductivity. Doping with organic solvents^{4,10} or treatments with particular salts, zwitterions, carboxylic or inorganic acids, polar organic compounds, or cosolvents can further increase the electrical conductivity. Doping and dedoping processes strongly affect oxidation level and thus carrier mobility and so increase the Seebeck coefficient and electrical conductivity.¹⁰ Power factors as high as $1,270 \mu\text{W m}^{-1} \text{K}^{-2}$,¹¹ and ZT of 0.42¹² at room temperature have been reported.

Reported values of ZT can be misleading due to material anisotropy and characterization challenges, and the record high ZT of 0.42¹² has recently been called into question.¹³ Samples used for thermal conductivity measurements were processed differently than samples for electrical conductivity and Seebeck coefficient measurements. Additionally, uncertainties inherent in extracting in-plane thermal conductivity using the 3ω method result in a large uncertainty range around the calculated ZT . Because thermal and electrical transport occurs in the same direction in a TE material, characterization of all TE properties should be along the same direction. Anisotropy of electrical conductivity in spin-coated PEDOT:PSS¹⁴ and a significantly high electron contribution to thermal conductivity¹³ result in higher in-plane thermal conductivity compared to the through-plane direction. The in-plane thermal conductivity of PEDOT:PSS thin films has since been reported to be higher than that measured by Kim *et al.*¹² in studies using different measurement techniques such as time-domain thermoreflectance,¹⁵ flash analysis,¹⁶ and a direct measurement using suspended microdevices.¹³ However, the materials in each study were processed differently, so direct comparisons between their results should be made with caution since processing methods affect properties.¹³

Electrical conductivity is a key property for TE performance, and the film morphology directly affects the performance of PEDOT:PSS films. PEDOT:PSS films exhibit a phase segregated morphology with PEDOT:PSS grains surrounded by shells of excess PSS. The PEDOT-rich grain cores are much more electrically conductive than the PEDOT-depleted grain boundaries; these boundaries are the main obstacle to charge transport in PEDOT:PSS. PEDOT-rich grains form elongated pancake-shaped islands that create an electrical percolation network in PEDOT:PSS. The orientation of these grains is affected by deposition techniques. Grains align parallel to the film plane in spin-coated samples, resulting in anisotropy of electrical conductivity of up to three orders of magnitude between in-plane and out-of-plane directions.¹⁴ For films deposited by inkjet printing, evaporation-driven internal convective flows lead to the coffee ring effect and orient grains both parallel and perpendicular to the film plane. The orientation reduces the out-of-plane to in-plane electrical conductivity ratio to 1.3 : 1.¹⁷

Charge-transport in conductive polymers at room temperature is governed by delocalized diffusion or phonon-assisted, localized hopping, that allows positive (bi)polarons to move between sites in response to vibrations surrounding the atoms.⁴ Both transport schemes are dependent on the morphology, crystallinity, doping levels, and the stacking and conformation manner of molecules. TE properties of conjugated polymers are dependent on carrier concentrations, the chemical structures of monomers and counterions, and the molecular arrangement. Optimization of TE properties is possible by controlling morphology and tuning carrier concentration, a technique demonstrated in 2011 by Crispin and coworkers¹⁸ and is now a routine step for optimizing polymer TE properties.⁴ Some small organic molecules, including charge transfer complexes or radical cation salts, and molecular semiconductors such as pentacene and fullerene films are also studied for their TE properties though research on these materials lags behind that of polymers.

The performance of organic TE materials is limited by relatively low power factors compared to inorganic counterparts. The most promising route to improving power factor is by

increasing carrier mobility.^{4,10} Notable developments are the following: (1) organic nanocomposites of conducting polymers and carbon nanotubes^{19–24} and graphene flakes,²⁵ and (2) organic–inorganic hybrid nanocomposites consisting of inorganic nanoparticles such as Bi₂Te₃, Sb₂Te₂, and Ca₃Co₄O₉, dispersed into a polymer matrix, most commonly PEDOT:PSS.¹⁰ Energy transport and conversion in hybrid nanocomposites are heavily influenced by interactions at the organic–inorganic interface where discrete molecular orbitals of organic molecules overlap with the continuum electronic states of metal and semiconductor nanoparticles.²⁶ TE properties in these composites depend on molecular and macromolecular parameters of both particle and polymer constituents together. Conduction can occur solely through the dispersed nanoparticles or the polymer host material, and there can be a conduction pathway between both constituents where π – π interaction between phases decreases the potential barrier at interfaces, facilitating charge transfer between the crystalline solid particles.²⁷ Carrier transport in a system of tellurium nanowires dispersed into PEDOT:PSS may occur through a highly conductive polymer region at the nanowire–polymer interface.²⁸ The electrical percolation network depends on the concentration, distribution, and morphology of solid particles whose arrangement may be affected by internal flows present in drying inks. Interfacial regions between solid particles and host polymers and the nature of bonding between them are poorly understood.²⁷

Inclusion of organic or inorganic nanoparticles into conducting polymers can substantially increase the Seebeck coefficient and electrical conductivity while having little effect on thermal conductivity. The phonon component of thermal conductivity in organic–inorganic composites is intrinsically low because of acoustic impedance and mismatch of vibrational densities of state at organic–inorganic interfaces. Additionally, these systems contain large numbers of randomly distributed boundaries, surfaces, and nanoscale structures of varying shape and size that effectively scatter phonons.²⁹

Physical properties of composites are often described with arithmetic averages of their components, so the upper bound of performance is limited by the best-performing individual compound of the composite. However, for organic–inorganic nanocomposites, several routes exist for overcoming this limitation and producing properties that surpass those of either constituent material. Such routes include carrier filtering at the organic–inorganic junction, density of states tuning through inclusions that produce trapped states, heterojunction charge transfer, decoupling of electrical conductivity and electron thermal transport in 1D systems, reduction of the lattice contribution of thermal conductivity, and structural alterations of organic material at organic–inorganic interfaces.²⁹ These hybrid nanocomposites combine the exceptional TE properties of inorganic semiconductors with the intrinsically low thermal conductivity³⁰ and ease of processing¹⁰ of polymers.

TE devices are conventionally made with traditional manufacturing techniques beginning with TE material synthesis via ball milling or melting/heating powders of constituent elements. Alloyed powders are then consolidated into ingots, diced, and metalized.

The resulting TE “legs” are bonded to electrical shunts on an insulating substrate. The traditional manufacturing process constrains the size, shape, and packing density of TE legs and can lead to chipping or formation of microcracks in brittle materials.^{5,7} Thin film TE materials consisting of superlattices and nanowires are made with manufacturing techniques common to the semiconductor industry. Processes for growth, deposition, etching, micro- and nanofabrication including chemical vapor deposition, molecular beam epitaxy, vapor–liquid–solid growth and electroless etching,⁷ pulsed laser deposition, and magnetron sputtering have been used.³¹ These processes are typically time-consuming and require expensive, specialized equipment.

Solution-based printing processes are attractive for large-scale fabrication because of their simplicity and affordability. Advantages relative to conventional manufacturing include simple patterning, material compatibility, and reduced energy input and material waste. Commercial demonstrations of printed TE devices are underway.^{32,33} This review covers four printing techniques—inkjet printing, direct write, screen printing, and stereolithography—which are currently used in depositing TE materials. Diagrams of each printing technique are shown in Figure 1. An overview comparing traditional and printing manufacturing techniques is presented in Table I. Here, we characterize scalability by (1) the ability to produce many devices rapidly and with minimal material waste during fabrication and (2) the ease of altering device design or scale. Techniques are compared using figures of merit for fabricated materials and devices. For inkjet and screen printing, several works did not measure thermal conductivity and report performance in terms of the power factor, σS^2 , where σ is electrical conductivity and S is the Seebeck coefficient. For these instances, ZT is calculated based on the reported power factor and an estimated thermal conductivity based on a weighted average of constituents of printed materials. For all cases, the estimate constitutes the lower bound for the ZT range in Table I. Examples of printed TE devices are shown in Figure 2. There are many reviews that explain the history and operation of printing techniques for electronic devices⁴⁰ and discuss specific techniques such as inkjet printing,^{34,41–44} dispenser printing,⁴⁵ screen printing,⁴⁶ and stereolithography.⁴⁷ This review focuses on the techniques' applications and challenges for TE materials and devices. Operation principles for each method are briefly explained along with particular advantages and challenges, followed by a review of recent work that used these techniques for printing TE materials.

TYPES OF INKS

Traditional inks used in printing processes carry pigment or dye to a substrate for the purpose of depicting images or text. They are typically water-based and exhibit Newtonian behavior (linear shear stress–strain rate relationship and constant viscosity with respect to the rate and duration of deformation).³⁴ Functional inks fulfill a purpose beyond graphical representation (e.g., electrically conductive printed tracks, chemical and biological sensors, semiconductor materials for thin field effect transistors, etc.). Two types of functional inks are reviewed here: multiphase solid particle dispersions and reactive precursor solutions. The first includes nanocomposite pastes with inorganic nanoparticles dispersed into a polymer matrix (e.g., bismuth

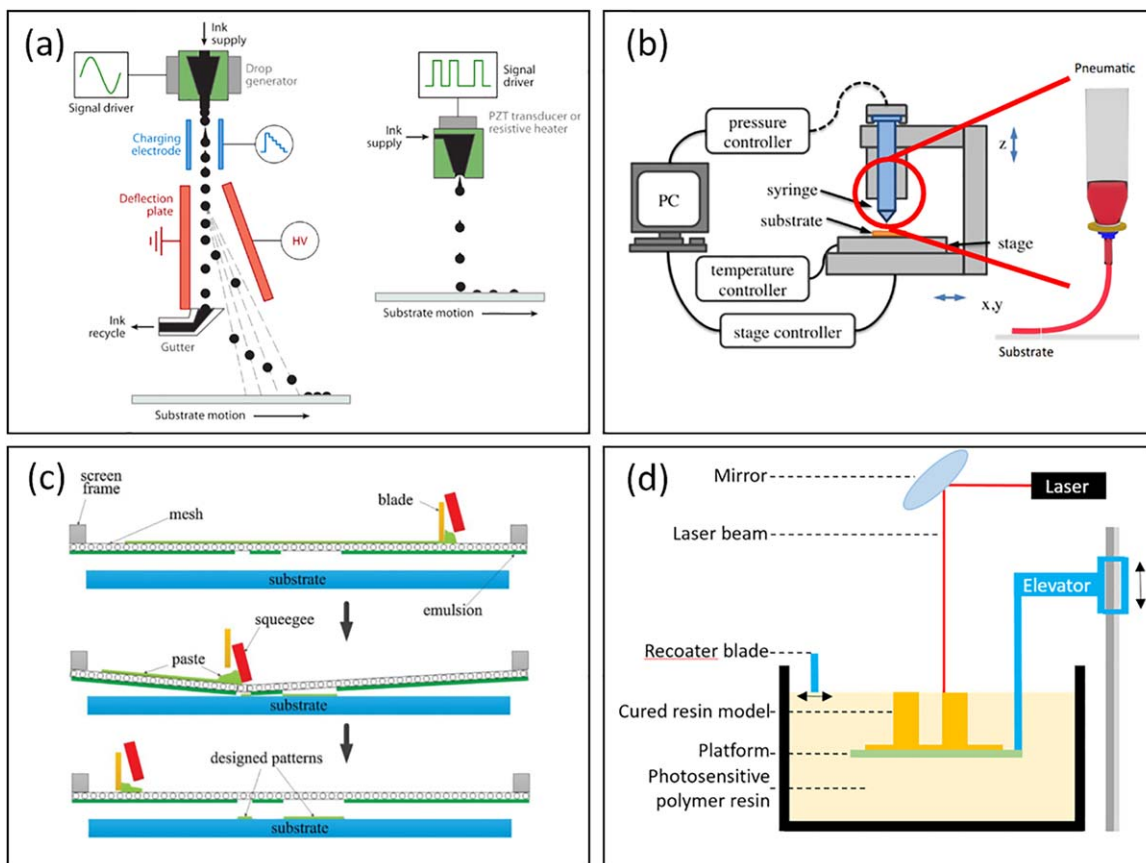


Figure 1. (a) Left: schematic of continuous inkjet printing. Right: thermal or piezoelectrically actuated, drop-on-demand inkjet printing. (Reproduced from ref. 34, with permission from [Annual Reviews].) (b) Schematic of dispenser printing. (Reproduced from refs. 35 and 36 with permission from [IOP Publishing] and [Cell Press].) (c) Diagram of screen printing. (Reproduced from ref. 37, with permission from [Elsevier].) (d) Diagram of stereolithography process. [Color figure can be viewed in the online issue, which is available at wileyonlinelibrary.com.]

telluride (Bi_2Te_3) and antimony telluride (Sb_2Te_3) particles in epoxy resins^{37,48} and colloidal suspensions of metal or semiconductor nanoparticles in organic solvents (e.g., zinc oxide (ZnO) nanorods⁴⁹ or silicon (Si) nanoparticles^{50,51} in ethylene glycol and aqueous dispersions of antimony bismuth telluride ($\text{Sb}_{1.5}\text{Bi}_{0.5}\text{Te}_3$) and bismuth tellurium selenide ($\text{Bi}_2\text{Te}_{2.7}\text{Se}_{0.3}$)).³¹ A post-processing annealing step is needed to recover functionality of the latter type. The second type of ink contains functional material precursors such as metal salts, complexes, and organo-metallic precursors dissolved in solution. These inks require a post-processing reaction⁵² which may take place between the ink and substrate, by different chemical species printed on top of one another,⁵³ or by annealing at moderate temperatures.⁵⁴

Both types of ink may exhibit non-Newtonian and viscoelastic behavior. The viscosity of non-Newtonian fluids varies with shear-rate, time, or both. Fluids whose rheological behavior involves an intrinsic time scale are termed viscoelastic and exhibit shear-thinning, strain-hardening, and yielding behavior (i.e., a transition from elastic to plastic deformation after a critical yield stress).³⁴ Such behavior can be problematic in an inkjet process. However, it is necessary for screen printing and some dispenser printing applications where the ink must flow under shear stress but quickly set up elastically upon relaxation.

Post processing is important for both types of ink. For nanocomposite pastes and nanoparticle dispersions, the printed films are subjected to an annealing process (thermal, photonic, microwave, etc.) to evaporate excess solvent and, at sufficiently high temperatures, sinter nanoparticles into a continuous, interconnected phase of functional material in which electrical and thermal energy carriers propagate. Some or all of the matrix phase of the ink may only serve to transport active material through the printing process. For devices fabricated on flexible substrates, annealing temperatures are limited by the glass transition temperature of the substrate. Because melting/sintering temperatures of the dispersed inorganic phase are higher than the glass temperature of the substrate (360–410 °C for a polyimide film),⁵⁵ the resulting film consists of many organic–inorganic interfaces which establish an electronic percolation network.

Design requirements for TE inks are stringent. The ink's rheological behavior must be suitable for the chosen deposition process and substrate. Both the concentration of a dispersed solid phase and agents used to stabilize against agglomeration and sedimentation affect ink rheology. The concentration of a dispersed solid phase must also be high enough to establish an electrical and thermal percolation network upon post processing, yet not so high as to clog or block nozzles or screens during the deposition process.

Table I. Summary of TE Device Manufacturing Methods Comparing the Traditional Manufacturing Approach to Printing Techniques

Printing technique	Material Class and Form	Patterning	Geometry	Post-processing	Scalability	Device performance [ZT range] ^a
Conventional TE Manufacturing	Inorganic semiconductor ingots	Automated or manual pick-and-place	Limited to simple geometries (rectangular)	Dicing, metallization, soldering	Limited	Up to 2, ⁵
Inkjet Printing	Hybrid ^b inks: nanoparticle dispersions, reactive precursors	Direct/digital	Thin planar	Required for solvent/stabilizer burnout-particle coalescence or chemical reaction	High	10 ⁻³ –0.25
Screen Printing	Hybrid pastes: dispersed solid phase, solvent, and binders	Mask/stencil	Thick planar	Required for binder burnout-particle coalescence	High	10 ⁻⁴ –0.61
Dispenser Printing	Hybrid pastes: dispersed solid phase, solvent, and binders	Direct/digital	Free-form	Required for binder burnout-particle coalescence	Low-med	0.013–0.19
Stereolithography	Hybrid photocurable resins	Direct/digital	Free-form	Required for binder burnout-particle coalescence	Low-med	0.12

Demonstrated/predicted device performance is presented in terms of the TE figure of merit, ZT

^aLower bounds are based on reported electrical conductivity, Seebeck coefficient and conservative estimates of thermal conductivity.

^bHybrid = inorganic-organic.

INKJET PRINTING

Inkjet printing is a solution-based, non-contact, additive, and mask-less deposition process in which materials are patterned at high speed and resolution. It is a well-understood and widely established technology with two main types, continuous and drop-on-demand. Continuous inkjet printers use plate electrodes to selectively charge individual droplets in a falling jet; charged droplets are deflected by an electric field onto a substrate while uncharged droplets fall into a gutter system for recycling. In drop-on-demand inkjet systems individual droplets are ejected by one of two mechanisms. In thermal drop-on-demand inkjet, small heating elements cause formation of vapor bubbles inside the print head near the nozzle. The rapid expansion and collapse of bubbles causes droplet ejection. In piezoelectric driven print heads, droplets are ejected by acoustic waves that are induced by mechanical deformation of the ink channel by a piezoelectric element. The piezoelectric transducer is controlled by a voltage signal optimized for droplet volume, velocity, and frequency. Inks for thermal inkjet printing are limited by their boiling point—heating elements must vaporize them—so piezo-driven inkjet dominates in applications for non-traditional, functional inks like TE materials.

Critical properties for inks in drop-on-demand printing are fluid density, viscosity, and surface tension. Droplet ejection results from superposition of consecutive acoustic waves that impart pressure pulses large enough to overcome viscous dissipation and the energy to create a new surface. The speed of sound in

the ink is dependent on its density. Viscosity acts to dampen excess acoustical waves and fluid movement to reset the fluid before the next pulse. Fluid viscosity also balances with surface tension in the ejected jet of fluid to ideally create a single droplet.⁵⁶ The dynamics involved in ejection of droplets by the piezo print head involve a highly complex coupling of electrical, acoustic, and fluid domains at varying length scales.⁴²

Challenges in Inkjet Printing

Despite the widespread use of inkjet technology for printed graphics and document applications, a number of challenges arise when printing electronic devices. Repeated ejection of individual droplets with uniform volume, velocity, and breakup behavior at high frequency depends on ink properties and conditions in the print head. Even when critical fluid properties are within optimal bounds for a particular printing system, problems like nozzle plate flooding, nozzle clogging, and erratic droplet ejection may persist.

TE inks often have particles suspended in a liquid. When the particles have diameters on the order of the nozzle's diameter, they can disturb the jetting process by forming an asymmetric meniscus, leading to the entrapment of air bubbles inside of the nozzle and deflecting subsequent droplets and clogging nozzles. Particles that are much smaller than the nozzle diameter do not affect fluid flow³⁴; however, they must be stabilized against aggregation with the use of surfactants or functionalized nanoparticles.⁵⁷ Colloidal nanoparticle suspensions, including TE material inks discussed here, are thermodynamically unstable

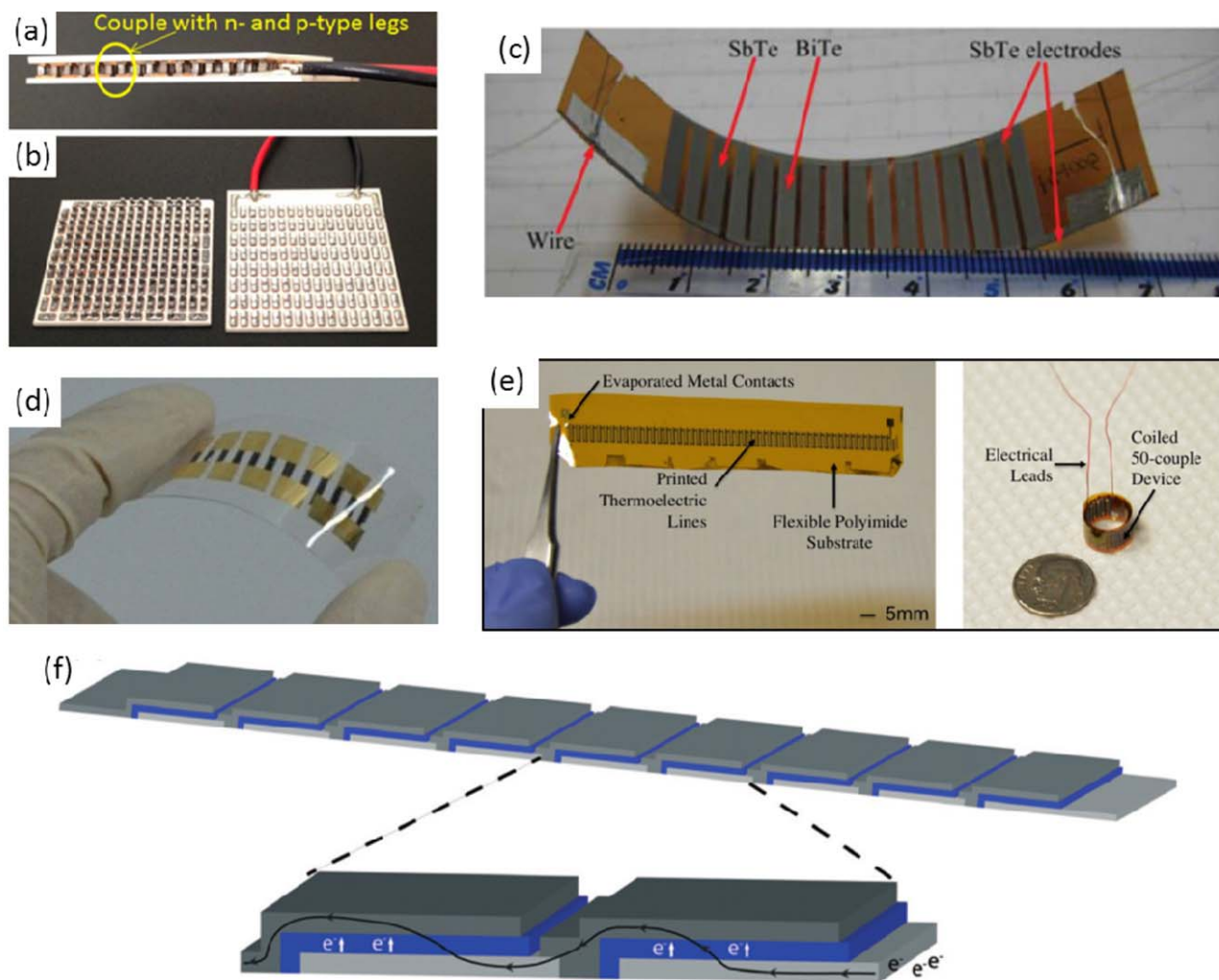


Figure 2. (a) Side view of an off-the-shelf TE module showing several TE “leg” couples. (b) Interior of a TE module with one substrate removed revealing electrical interconnects and solder joints. Module is approximately 1×1 in. and is supplied by Marlow Industries, Inc. (Reproduced from ref. 7 with permission from [Elsevier].) (c) Example of inkjet-printed TE generator on a flexible substrate. (Reproduced from ref. 38 with permission from [Royal Society Publishing].) (d) Example of screen-printed TE generator on a flexible substrate. (Reproduced from ref. 37 with permission from [Elsevier].) (e) Left panel: TE generator dispenser-printed on flexible substrate. Right panel: Coiled up TE generator. (Reproduced from ref. 35 with permission from [Elsevier].) (f) Schematic of a device architecture that uses only one TE material, fabricated in a roll-to-roll, rotary screen printing process. (Reproduced from ref. 39 with permission from [Society of Chemical Industry].) [Color figure can be viewed in the online issue, which is available at wileyonlinelibrary.com.]

due to high surface energy of the solid phase, and they exhibit pronounced Brownian motion.⁵⁸ Stability mechanisms are broken into two types, steric and electrostatic as depicted in Figure 3(b). Steric stabilization is achieved by polymers adsorbed onto particles whose branched structure hinders two particles from contacting each other. Electrostatic stabilization results from the development of a surface charge through one or more of several mechanisms including dissociation of surface charged species, preferential adsorption of ions, accumulation or depletion of electrons at the surface, and physical adsorption of charged species onto the surface.^{57,59}

Many functional ink formulations exhibit non-Newtonian or viscoelastic behavior. Inks with inorganic TE nanoparticles suspended in a Newtonian liquid vehicle and stabilized with polymeric additives are likely to exhibit viscoelastic behavior. The

viscosity–shear rate relationship of varying fluid types is depicted in Figure 3(c). During droplet ejection a wide range of shear rates are experienced from ~ 0 to 10^6 s^{-1} ,^{60,61} so large fluctuations in viscous behavior are possible and affect printability. Even in small concentrations, polymeric additives affect droplet formation; for example, they delay the break-up of drops compared with Newtonian inks. The liquid filament connecting a forming droplet to the fluid reservoir resists thinning because of extensional strain-hardening that increases local stresses and counteracts capillary pressure. When break-off does occur, the filament can form smaller satellite droplets, landing on the substrate in an uncontrolled manner. Satellite droplets are undesirable and reduce the quality of printed patterns.³⁴

The resolution and uniformity of printed features is particularly important for printed, flexible, electronic devices. For optimal

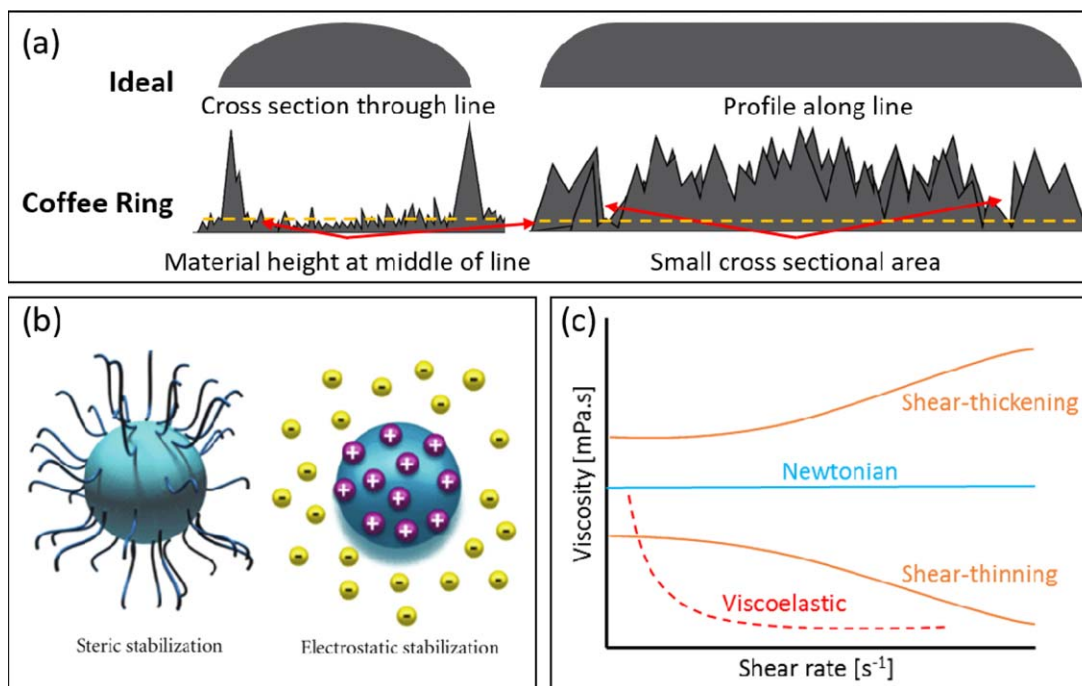


Figure 3. (a) Top: Ideal cross section and profile of a material in a dried printed feature. Bottom: Resulting cross-section and profile of a dried printed feature with the coffee ring effect. (b) Depictions of steric (left) and electrostatic (right) stability mechanisms for dispersed nanoparticle systems. (Reproduced from ref. 57 with permission from [Hindawi Publishing Corporation].) (c) Examples of the shear rate-dependent viscosity of different types of fluids. [Color figure can be viewed in the online issue, which is available at wileyonlinelibrary.com.]

electrical performance, conductive features should have a uniform cross-section to minimize resistance, so the substrate–liquid interaction and drying behavior are important for the functionality of the printed device. A well-known issue is the coffee ring effect whereby most solute is deposited at the periphery of the droplet footprint during solvent evaporation, depicted in Figure 3(a). This causes variation of cross-sectional area and limited connectivity between solid particles.

For a perfectly flat, defect free surface with no contact angle hysteresis, the contact point of the liquid–gas–surface interface will recede steadily during evaporation. The contact angle remains constant, and solute will be distributed equally across the droplet’s footprint. Realistically, the contact line becomes pinned at defects so evaporating liquid must be replenished from the interior of the droplet⁶² causing an internal flow that carries and deposits solute to the periphery. The coffee ring effect is generally undesirable because it leads to a highly non-uniform profile for printed features; however, some applications can utilize the effect for assembling macromolecular species or creating transparent conductive films.^{63–65} Methods of mitigating the coffee ring effect include electrowetting,⁶³ surfactant-induced Marangoni flows⁶⁴ and eddies,⁶⁶ and particle trapping at the liquid–gas interface due to enhanced hydrophobicity of oppositely charged surfactant-particle systems.⁶⁷

As discussed in the introduction, the coffee ring effect influences TE properties of PEDOT:PSS; anisotropy of electrical conductivity arises due to orientation of elongated, pancake-shaped, electrically conductive grains.^{14,17} The effect limits control and repeatability of printed features. As a TE device consist

of many pairs of thermocouple legs, consistency in the geometry of printed features in one device and across many devices is desirable.

A critical challenge for printed TEs relates to the thermal resistance of the active material compared to that of other device components. Increasing the temperature difference across the active TE material improves TE device performance, so a high thermal resistance is desirable. Because the thickness and thermal conductivity of typical substrates are on the same order of magnitude as those of organic TE materials, a significant temperature drop across the substrate occurs, decreasing the efficiency of printed TE devices. Performance is further reduced by electrical interconnect resistances, which become significant for thin TE elements.⁶⁸ Typical layer thicknesses of inkjet-printed TE nanoparticle inks are in the range of ~ 100 – 500 nm per layer^{49–51} compared to common substrate thicknesses of 10 – 100 μm ,⁵⁵ so multiple printing passes (2–150 passes in work reviewed here) and intermittent drying times are required, considerably decreasing throughput for large-scale manufacturing processes.

Summary of Inkjet Printed Material and Devices

Multiple groups have fabricated TE devices with inkjet printing using hybrid inorganic–organic inks. Their material synthesis methods, device architectures, and highlighted results relevant for TE power generation are explained below. The TE properties of materials and devices printed with inkjet are compared in Table II. In most cases, the thermal conductivity of the material is not measured, so the TE figure of merit, ZT , is not reported. Table I includes our conservative estimates of ZT . There is a

Table II. Comparison of TE Properties of Materials and Devices Fabricated via Inkjet Printing

Material	Annealing method	Thermal conductivity ($W m^{-1} K^{-1}$)	Electrical conductivity ($S m^{-1}$)	Seebeck coefficient ($\mu V K^{-1}$)	Power factor ($\mu W m^{-1} K^{-2}$)	ZT	Power produced (nW)	References
Aqueous $Sb_{1.5}Bi_{0.5}Te_3$ ink	RTA, 400 °C, 30 min, Ar	—	2000	177 ± 5 at 50 °C	77	—	—	[31]
Aqueous $Bi_2Te_{2.7}Se_{0.3}$ Ink	RTA, 400 °C, 30 min, Ar	—	6000	-139 ± 2 at 50 °C	183	—	—	[31]
PEDOT:PSS/ZnO nanorods	RTA, 150 °C	—	—	—	—	—	11, 5 TC ^a	[49]
poly[Cu _x (Cu-ett)]/PVDF/DMSO	RTA, 80–110 °C, 10 h, vacuum	—	550 ± 100	53 ± 2 at 127 °C	1.6	—	45, 6 TC ^a	[38]
poly[K _x (Ni-ett)]/PVDF/NMP	RTA, 80–110 °C, 10 h, vacuum	—	520 ± 50	-60 ± 10 at 127 °C	1.6 ^b	—	45, 6 TC ^a	[38]
PEDOT-Tos	RTA, 110 °C	0.37 ± 0.07	8000	200	326	0.25	128, 54 TC ^a	[18]

^aTC = number of thermocouples.^bDiscrepancy between reported values and figure in paper, this value is taken from the figure.

characterization need in this nascent area of polymer-based TE devices to measure thermal conductivity and ZT.

The first thin film TE generator fabricated by inkjet printing was demonstrated in 2014.³¹ Aqueous dispersions of $Sb_{1.5}Bi_{0.5}Te_3$ and $Bi_2Te_{2.7}Se_{0.3}$ nanoparticles were printed over silver contacts in 150 layers and annealed in Ar/H₂ gas at 400 °C for 30 min. The maximum power factor for the $Sb_{1.5}Bi_{0.5}Te_3$ film was $\sim 77 \mu W m^{-1} K^{-2}$ at 75 °C, and the $Bi_2Te_{2.7}Se_{0.3}$ film was $183 \mu W m^{-1} K^{-2}$.

A unique approach to printing organic–inorganic nanocomposites is to deposit alternating layers of conductive polymer precursor inks and an ink with dispersed inorganic nanoparticles. This avoids proceeding *in situ* reactions and the need for mechanical dispersion in ink production. The approach was demonstrated by printing 2- and 4-film structures with alternating layers of PEDOT:PSS ink and ZnO nanorods dispersed in ethylene glycol. The 4-film structures had a more homogenous cross-section leading to an increased power factor over the 2-film systems.⁴⁹

Compared with other organic TE materials, excellent TE properties of 1,1,2,2-ethenetetrathiolate(ett)–metal coordination polymers poly[Ax(M-ett)] (A = Na, K; M = Ni, Cu) have been demonstrated with ZT values of 0.2 for n-type poly[Kx(Ni-ett)] and 0.01 for p-type poly[Cux(Cu-ett)] at a temperature of 400 K.⁶⁹ These polymers are insoluble and infusible. Polymer composite synthesis via ball milling is a viable solution for p- and n-type composite coordination polymers composed of poly[Cu_x(Cu-ett)]/Poly(vinylidene fluoride) (PVDF)/dimethyl sulfoxide (DMSO) and poly[K_x(Ni-ett)]/PVDF/N-methyl-2-pyrrolidone (NMP). TE properties of both films depended on drying time and PVDF weight ratio. Power factors of 1.92 and 1.58 $\mu W m^{-1} K^{-2}$ at 400 K were achieved for n- and p-type composites, respectively. A flexible, 6 thermocouple device was inkjet-printed and produced a maximum output voltage of 15 mV and short circuit current of 3 μA for a temperature difference of 25 °C. The maximum power output was 45 nW for a load resistance of 5 k Ω .³⁸

The power factor of PEDOT-Tos was optimized by controlling the oxidation level with exposure to tetrakis(dimethylamino)-ethylene (TDAE) vapor in an inert atmosphere. Between oxidation levels of 36 and 15%, the electrical conductivity dropped from 300 $S cm^{-1}$ to $6 \times 10^{-4} S cm^{-1}$. The Seebeck coefficient increased by a factor of 20, reaching 780 $\mu V K^{-1}$ at the lowest oxidation level. The optimum oxidation level was 22% corresponding to a power factor of 326 $\mu W m^{-1} K^{-2}$. Thermal conductivity was $0.33 \pm 0.1 W m^{-1} K^{-1}$ and $0.37 \pm 0.07 W m^{-1} K^{-1}$ for the vertical (out-of-plane), and lateral (in-plane) directions, respectively. A 54 leg TE module was inkjet-printed; p-type legs were made with PEDOT-Tos while n-type legs were a mixture of an organic conducting salt, tetrathiafulvalene-tetracyanoquinodimethane (TTF-TCNQ), and polyvinylchloride in toluene. The maximum power output of the device was 0.128 μW for a temperature difference of 10 °C.¹⁸

The use of nanoparticle inks necessitates a post-processing annealing step in which excess solvent, binder, and stabilizing

materials are burned off, and nanoparticles sinter together, forming a continuous network and recovering bulk properties. The most common method is Rapid Thermal Annealing (RTA) whereby printed features are exposed to elevated temperatures. Other methods include microwave, photonic, laser, and plasma sintering.⁷⁰ Microwave sintering differs from the others in that heat is generated within the material via dielectric interaction,⁷¹ rather than irradiation, conduction, or convection. Much research on printed functional materials studies material properties as a function of annealing methods and parameters such as time, temperature, and atmosphere. For inkjet-printed Si nanoparticle inks, RTA has been compared to microwave⁵⁰ and photonic⁵¹ annealing methods. Parameters included the inert and reducing atmospheres, nanoparticle surface functionalization with poly(methacrylic acid) (PMA), and the amplitude, pulse length, and duty cycle of the photonic system. Nanoparticles without PMA melt at a higher temperature (1200 °C) than functionalized nanoparticles (800 °C)⁵¹ because of a higher oxidation state. The evolution of stress in the films was found to be independent of annealing method, following a linear increase of tensional stress up to 800 °C beyond which stress was compressive. Tensional stress was caused by variation in thermal expansion between Si film and quartz substrate. Compressive stress resulted from increased rate of oxidation in grain boundaries. Samples annealed in a reducing atmosphere⁵⁰ or with the photonic method⁵¹ exhibited less stress. Scanning electron microscopy images confirm strong dependence of microstructural evolution on temperature; however, no clear difference between microwave and RTA annealing was observed.⁵⁰ Photonic sintered films were discontinuous due to possible blow off from processes with high dissipated power.⁵¹ Electrical conductivity of films evolved as a function of annealing temperature for RTA and microwave methods, reaching a peak for RTA at 850 °C but decreased thereafter due to oxidation and crack formation. Calculated thermal conductivity increased with temperature for both RTA and microwave methods.⁵⁰ The small change in thermal conductivity for photonic sintered films suggests the absence of grain coarsening which is advantageous for applications where nanoscale grains are preferred, such as keeping thermal conductivity low in TE devices.⁵¹

SCREEN PRINTING

In screen printing, ink is deposited through a porous printing plate made from a woven mesh of synthetic fabric threads or metal wire that is affixed to a rigid frame. The pattern is defined by a mask or stencil. Bidirectional tension is applied to the mesh to create a semi-rigid planar surface that has three functions: (1) meter fluid flowing through it under pressure, (2) provide a surface to shear columns of viscous fluid that form during transfer to substrate, and (3) provide structural support for the stencil. A flexible plastic blade pushes into the screen until it makes contact with the substrate. The blade then sweeps horizontally, scraping a pool of ink across the screen, and pushing it through openings in the mesh and onto the substrate in a pattern defined by the stencil. Screen printing can be applied in a roll-to-roll process using a cylindrical frame and screen that enclose the ink deposition and blade inside.⁷² TE properties of

materials and devices fabricated with screen printing are compared in Table III.

Challenges in Screen Printing

As discussed for inkjet printing, achieving sufficient TE material thickness relative to that of the substrate is problematic. The thinnest substrates feasible for roll-to-roll printing are ~10–20 μm, and, while depositing relatively thick wet layers of ink is possible with screen printing, the ink must have sufficient viscosity to hold its form and will require longer drying times,³⁹ increasing production costs. Large wet thicknesses are also problematic when good control of pattern morphology is required.⁷⁸ Dry ink layers greater than 20 μm are prone to delamination or cracking, especially for flexible devices.³⁹ The negative of the mesh structure can be reproduced in the surface of printed patterns. This significantly increases surface roughness.^{78,79} For vertical structures the rough top surface increases the contact resistance between it and subsequent layers. Another problem arises for inks made with volatile solvents. In an industrial setting, the printing apparatus could be covered in ink and exposed to air for several hours at a time during which evaporating solvents can cause buildup of dry ink on the screen printing mask, deteriorating the resolution of printed patterns.⁷⁸ This adds another constraint when formulating TE inks since the vapor pressure of the final formulation must be sufficiently low.

Summary of Screen Printed Material and Devices

Like inkjet-printed nanoparticle inks, the inorganic–organic pastes used in screen printing require an annealing step to recover functionality. The electrical and microstructural characteristics of screen printed films comprised of either $\text{Ca}_3\text{Co}_4\text{O}_9$ or $(\text{ZnO})_5\text{In}_2\text{O}_3$ were investigated as a function of firing temperature. Inks were printed onto an alumina substrate in three layers and fired at 900 and 920 °C for $\text{Ca}_3\text{Co}_4\text{O}_9$ and 1250, 1300, 1350 °C for $(\text{ZnO})_5\text{In}_2\text{O}_3$. The highest electrical resistivity, Seebeck coefficient, and calculated power factor for $\text{Ca}_3\text{Co}_4\text{O}_9$ were 13.7 mΩ cm, 156 μV K⁻¹, and 1.6×10^{-4} W m⁻¹ K⁻², respectively. The same properties for the $(\text{ZnO})_5\text{In}_2\text{O}_3$ material were 0.720 Ω cm, -176 μV K⁻¹, and 1.4×10^{-6} W m⁻¹ K⁻², respectively. However, the lowest resistivity for $(\text{ZnO})_5\text{In}_2\text{O}_3$ required a firing temperature of 1350 °C at which point a reaction took place between ZnO and the substrate forming an interfacial ZnAl_2O_4 phase. Sublimation of ZnO also occurred causing In_2O_3 rich grains at the surface of the film.⁷³

By placing excess tellurium powder into the chamber for RTA, the carrier mobility of a screen printed Sb_2Te_3 thick film was increased threefold, and the power factor nearly doubled. The change in properties is attributed to suppression of Sb_2O_3 formation during the annealing step. Electrical and thermal conductivity increased with annealing time while Seebeck coefficient remained constant. Both electrical and thermal conductivity were four times less than values reported for bulk Sb_2Te_3 . Low thermal conductivity is due to high film porosity.⁷⁴

A similar result was found for screen printed Bi_2Te_3 films annealed in the presence of excess material powders. Electrical conductivity increased with annealing temperature up to 500 °C and decreased thereafter due to evaporation of Te powders,

Table III. Comparison of TE Properties of Materials and Devices Fabricated via Screen Printing

Material	Annealing method	Thermal conductivity ($W m^{-1} K^{-1}$)	Electrical conductivity ($S m^{-1}$)	Seebeck coefficient ($\mu V K^{-1}$)	Power factor ($\mu W m^{-1} K^{-2}$)	ZT	Power produced (nW)	References
$Ca_3Co_4O_9$	RTA, 900–920 °C	—	7400	156	1.6×10^{-4}	—	—	[73]
$(ZnO)_5In_2O_3$	RTA, 1250–1350 °C	—	139	–176	1.4×10^{-6}	—	—	[73]
Sb_2Te_3	RTA w/excess Te	0.9–1.1	$7.2\text{--}12 \times 10^4$	90–100	—	0.32	—	[74]
Bi_2Te_3	RTA, 530 °C, 10 min in N_2 , pressure	1	55,000	140	—	0.32	—	[75]
Sb_2Te_3	RTA, 500 °C, 10 min in N_2 , pressure	1.25	130,000	99	—	0.29	—	[75]
Bi_2Te_3	RTA w/excess Te	0.9–1.1	2600	137.5	2100	0.61	—	[76]
Sb_2Te_3 /binder A	RTA, 250 °C, 3 h	—	7800	–134.38	141	—	444 ^a , 8 TC	[37]
Bi_2Te_3 /binder B	RTA, 250 °C, 3 h	—	19,920	103.67	215	—	444 ^a , 8 TC	[37]
PEDOT:PSS	—	—	—	0.044 ^b	—	—	0.054 ^b	[39]
PEDOT:PSS	RTA, 150 °C, 30 min	—	55,000	25	34	0.01 ^c	50,000, 300 TC	[77]

^aTE devices used Binder B and no ISP treatment.³⁷^b10 windings and no adhesive.³⁹^cZT calculated using thermal conductivity from.¹²

while Seebeck coefficient increased slightly with temperature. The effect of dwell time at 500 °C from 0 to 60 min was similar to that of annealing temperature, with power factor increasing initially up to 15 min and decreasing thereafter. The maximum power factor was $2.1 \text{ mW m}^{-1} \text{ K}^{-2}$, an order of magnitude greater than samples annealed without excess material powder present. Thermal conductivity was measured in the range of $0.9\text{--}1.1 \text{ W m}^{-1} \text{ K}^{-1}$ and showed little dependence on dwell time. A ZT of 0.61 was calculated at room temperature.⁷⁶

The effect of two binder systems (A and B), electrical contacts of either commercial silver paste or Sb_2Te_3 paste, and a cold isostatic press post-process were studied for screen printed Bi_2Te_3 and Sb_2Te_3 pastes. Binder system A was a 4,4'-Isopropylidenediphenol-epichlorohydrin-based epoxy, and binder system B was an epichlorohydrin-polyglycol-based epoxy. Films with binder B had less electrical resistance compared to A. However, unlike A, system B showed no improvement in properties after cold isostatic pressing due to its high compressive strength (160 MPa for B, 16 MPa for A). Cold isostatic pressing reduced both the contact resistance and the resistivity of the TE materials due to a reduction in size and quantity of voids within the materials. Contact resistance was lower for Sb_2Te_3 contacts as compared to silver contacts (2.7–7.3 k Ω). The optimal combination of materials and processes for the screen-printed TE generators was Bi_2Te_3 with binder B, Sb_2Te_3 with binder A, Sb_2Te_3 contact electrodes, and cold isostatic pressing of the assembly. The Seebeck coefficient, electrical resistivity, and power factor for the Bi_2Te_3 films were $-134.38 \mu V K^{-1}$, $1.28 \times 10^{-2} \Omega \text{ cm}$, and $1.41 \mu W K^{-2} \text{ cm}^{-1}$, respectively, while the same for the Sb_2Te_3 material in binder A was $103.67 \mu V K^{-1}$, $5.01 \times 10^{-3} \Omega \text{ cm}$, and $2.15 \mu W K^{-2} \text{ cm}^{-1}$.³⁷

The feasibility of high throughput, roll-to-roll processing was demonstrated by printing 18,000 serially connected junctions via rotary screen printing of PEDOT:PSS in-between silver top and bottom electrodes that were printing with a different method, flexography. The unique architecture requires only one TE material (n- or p-type), see Figure 3f. The relatively large thickness of the substrate and adhesive layer compared to the active TE layer (60 μm , 60 μm , and 1.2 μm , respectively) limited the performance. The maximum power output achieved was 54 pW for an overall temperature difference of 70 °C.³⁹

Polymer-based TE generators have been modeled and demonstrated. A flexible TE generator intended for harvesting body heat was fabricated via screen printing. The output power density of 0.38 mW cm^{-2} for a temperature difference of 50 K is tens of times higher than previously reported devices. The wearable TE generator was thin ($\sim 500 \mu\text{m}$) and light ($\sim 0.13 \text{ g cm}^{-2}$) having output power per unit weight of 28 mW g^{-1} .⁷⁵ The performance of a polymer-based TE generator with a cylindrical architecture was evaluated in which the fill factor F is greater than unity, $F > 1$. Fill factor is the ratio of area covered by TE material to the hot-side heat exchanger area. Heat spreading in the TE material occurs when $F > 1$ which increases efficiency by slowing down heat conduction. A model was developed for determining optimum device geometries and a prototype demonstration is underway in which disks of p-type

(PEDOT:PSS with dispersed Te nanowires) and n-type (poly [Kx(Ni-ett)]/PVDF/DMSO) are screen printed and stacked between separation layers that both electrically isolate the disks and create a current path.⁶⁸

The first example of powering a practical device with a TE generator containing conducting polymers was reported in 2014. Arrays of aqueous PEDOT:PSS were screen printed onto paper and electrically connected via a screen printed silver paste. After annealing at 150 °C for 30 min in air, the electrical conductivity and Seebeck coefficient of the printed material was 550 S cm⁻¹ and 25 μV K⁻¹, respectively at 200 °C. Three hundred of the arrays on paper were sandwiched between copper plates and connected either in series or in parallel to create a large area TE module. For a temperature difference of 100 K, the module produced a power output greater than 50 μW and powered an LED. The silver/PEDOT:PSS interface was thermally unstable resulting in a decrease of power by roughly half its initial output when operated at elevated temperatures for 100 h. X-ray photoelectron spectroscopy indicated PSS segregation on the silver/PEDOT:PSS interface leading to increased contact resistance.⁷⁷

DISPENSER PRINTING

Here, the term dispenser printing describes filament-extrusion-based deposition pattern generation techniques. Specific processes include robocasting, fused deposition, and micropen writing.⁸⁰ For each one, a computer controlled x-y stage translates the substrate under a nozzle that dispenses a continuous filament of ink slurry in a pattern defined by a CAD file. A feedback control system controls the distance from the nozzle tip to the substrate, the driving pressure, and the translation speed to enable conformal writing with excellent control of feature geometry.⁴⁵ With careful control of rheological behavior, ink composition, and printing parameters, 3D structures consisting of continuous solids, high aspect ratio parallel walls, and features that span gaps are possible. The ink properties must be such that the inks flow through the nozzle and immediately set up for shape retention, especially if they are to span gaps in underlying layers. A high colloid volume fraction minimizes drying-induced shrinkage after assembly.⁸⁰ The maximum density of conductive lines on a printed device indirectly describes the upper limit of its functionality. With more lines and active/passive components per printed area, there is more potential for functionality in a single device, so the minimum printable feature size is important. For dispenser printing of sol-gel and colloidal ceramic inks, features down to 250 nm and 200 μm have been demonstrated.⁸¹ TE properties of materials and devices fabricated by dispenser printing and stereolithography are compared in Table IV.

Challenges of Dispenser Printing

Design of concentrated inks suitable for printing at the micro-scale is not trivial. Bulk rheological behavior of inks are highly sensitive to particle size, shape, concentration, and stability against aggregation due to inter-particle attractive forces. Aggregation as a result of such forces can cause nozzle clogging or require excessive pressure to induce flow. However, these inter-

Table IV. Comparison of TE Properties of Materials and Devices Fabricated via Dispenser Printing or Stereolithography^a

Material	Annealing method	Thermal conductivity (W m ⁻¹ K ⁻¹)	Electrical conductivity (S m ⁻¹)	Seebeck coefficient (μV K ⁻¹)	Power factor (μW m ⁻¹ K ⁻²)	ZT	Power produced (nW)	References
Sb ₂ Te ₃ /Bi ₂ Te ₃	-	-	-	23.56	-	-	1.54, 1 TC	[48]
Bi ₂ Te ₃	-	0.48	800	-159	0.20 × 10 ⁻⁴	0.0126	-	[82]
Bi _{0.5} Sb _{1.5} Te ₃	-	0.52	1440	272	1.07 × 10 ⁻⁴	0.0615	-	[82]
Sb ₂ Te ₃	RTA, 250 °C, Ar	0.24	4000	170	120	0.18	-	[35]
Bi ₂ Te ₃	RTA, 250 °C, Ar	0.24	3000	-160	110	0.19	10.5, 50 TC	[35]
Bi _{0.5} Sb _{1.5} Te ₃	RTA, 350 °C	0.25	4800	147	-	0.12	-	[83]

^a Last row is for material printed via stereolithography.

For the column showing power produced, TC indicates the number of TE couples measured to obtain the power value.

particle attractive forces are important for set up of the ink's structure post deposition.

Summary of Dispenser Printed Materials and Devices

Up to this point all discussed TE devices have been thin and in a planar orientation, meaning heat transport is parallel to the substrate. A thick, vertically fabricated 3D TE generator, where heat is intended to flow perpendicular to the substrate, was made with a custom-made dispenser printing system and pastes containing inorganic Bi_2Te_3 and Sb_2Te_3 materials. The device was printed onto a polyimide film pre-patterned with silver bottom electrodes. Ultra-violet light curable polymer blocks (OG675 epoxy, EPO-TEC) were printed between TE material blocks to support a top silver electrode. Silver-TE contact resistance dominated the internal resistance of the printed device; there may have been a chemical reaction between silver electrodes and uncured TE materials. For an 8 thermocouple device, the Seebeck coefficient, and maximum power output were $23.56 \mu\text{V K}^{-1}$ and 1.54 nW , respectively.⁴⁸

A different approach for fabricating a TE device using dispenser printing incorporating a polymer mold to define the geometry and placement of TE materials was demonstrated. The method was motivated by a calculated optimal leg length of 100–200 μm suggested by design studies. Inorganic-epoxy composite inks were synthesized with n-type Bi_2Te_3 and p-type $\text{Bi}_{0.5}\text{Sb}_{1.5}\text{Te}_3$ particles dispersed into an epoxy resin comprised of bisphenol f, an anhydride-based hardener, 2E4MZCN (Sigma-Aldrich, Inc.) catalyst, and butyl glycidyl ether to adjust viscosity. Printed lines were cured at 250°C in argon. The ZT for the n- and p-type composite films at 300 K were 0.0126 and 0.0615, respectively.⁸²

Chen *et al.* also fabricated planar TE generators via dispenser printing using pastes with n-type Bi_2Te_3 and p-type Sb_2Te_3 powders and the same epoxy resin described above,⁸² with the exception of a phosphate-based accelerator (AC-8, Broadview Technologies, Inc.) used for a catalyst. The TE device was fabricated with gold bottom contacts via shadow mask evaporation on a polyimide substrate followed by n- and p-type elements dispenser printed and cured in argon at 250°C . Thermal conductivity of both composite films was $0.24 \text{ W m}^{-1} \text{ K}^{-1}$. The maximum ZT for the n- and p-type composites were 0.18 and 0.19, respectively. A 50 thermocouple prototype was printed, rolled into a coil and sealed with polyimide tape. For a temperature difference of 20 K and at matched load resistance, the fabricated device produced $10.5 \mu\text{W}$ at $61.3 \mu\text{A}$ and 171.6 mV .³⁵

STEREOLITHOGRAPHY

Stereolithography is a liquid-based process in which a photosensitive polymer resin is cured or solidified when exposed to an ultraviolet laser.⁸⁴ First, a 3D CAD model is translated into a Standard Tessellation Language file, which breaks the model into triangular facets. Intersection points of horizontal slices and the edges of facets are then interpreted by the printing software in creating a pattern for each layer. A platform that anchors and supports the workpiece is submerged into a resin vat, and a UV laser solidifies a cross-section of the model. After each layer, the platform is lowered by an amount equal to the

thickness of each layer. The excess resin is drained (and sometimes reused), leaving only the 3D object.⁸⁴ Microstereolithography is a high-resolution process capable of layers 1–10 μm thick.^{81,85} The minimum resolution is limited by the viscosity and surface tension of the resin. A two-photon polymerization process was developed to overcome this limitation⁸⁶; two photons are needed to initiate polymerization. Resolution is considerably increased because the irradiance of the laser is only high enough to activate the photoinitiator near the center of the beam.⁸¹ By careful focus of femtosecond lasers in two-photon-polymerization processes, spatial resolutions down to $\sim 100 \text{ nm}$ are achievable, and with a long laser-exposure technique, sub 30 nm structures have been demonstrated.⁸⁷

Powders of other materials such as ceramics⁸⁸ or inorganic TE materials⁸³ may be suspended in the liquid resin where the photosensitive resin acts as the structural support and is removed during a post-processing annealing step. A key advantage of stereolithography fabrication is structures of any self-supporting geometry may be created. For TE devices this feature enables unique leg geometries that could increase power density. For example, legs with a smaller cross-sectional area at the hot side than that at the cold side cause heat to spread out, optimizing performance from a $\$/\text{W}$ standpoint.⁶⁸ TE properties of materials printed via stereolithography are compared to those printed with the dispenser technique in Table IV above.

Challenges of Stereolithography

For TE devices made from solid particle dispersions in resins, the final part density is relatively low with many pores and particle-particle contacts. The porous structure would have high thermal resistance, which is desirable for TE devices, but also high electrical resistance, reducing device performance. Using two or more materials to create one part with stereolithography is possible but not practical as it requires completely draining the vat of one resin, filling the vat with a different resin,⁸⁴ and aligning the surface of liquid with the top of the part. The feature article by Wicker and MacDonald details recent developments of stereolithography systems capable of printing multiple materials.⁸⁹ Fabrication of a complete TE generator with both n- and p-type legs would require such a process. Because the cured resin is the scaffold for a dispersed phase of functional particles, it must be removed, and particles must coalesce in a post processing annealing step to recover functionality. The parameters for this annealing step (temperature, time, and atmosphere) are different for each material, so creating a process that either works for all materials or multiple processes that only significantly affect one material will have additional challenges.

To anchor a layer of resin to the previous one, the resin is over-cured by a specified thickness into the underlying layer. The effect—called “print-through”—compounds, resulting in thicker layers near the bottom of structures. The thickness of layers near the top and bottom of printed structures differ by on average 20–40 μm .⁹⁰ This effect is especially pronounced for overhanging structures, reducing their resolution and introducing errors.⁸⁴ Horizontal variation of resolution results because of changes in the spot size, shape, and laser focus as it is deflected at different angles. Differences of wall thicknesses as large as

163 μm were observed for grid structures printed at the center and corners of the platform.⁹⁰ Uniformity of resolution is important for producing TE devices on a large scale so that all device elements conform to design tolerances. For applications with features and tolerances much greater than 150 μm , this issue may be minimal.

Similar to the problem in screen printing where the mesh pattern is produced on the surface of features, the scanned line shape can be seen on parts printed with stereolithography resulting in a ribbed surface. Smooth surfaces in TE materials are desirable since thermal and electrical contact resistances deteriorate device performance. The surface may be smoothed by a finishing process usually done by hand,⁸⁴ but this can introduce irregularity from part to part and significantly decrease throughput.

Summary of Stereolithography Printed Materials

Amorphous TE materials have been fabricated via stereolithography with p-type $\text{Bi}_{0.5}\text{Sb}_{1.5}\text{Te}_3$ alloy powders of varying concentration dispersed in a custom photoresin comprised of 3,4-epoxycyclohexylmethyl-3,4-epoxycyclohexane carboxylate, diluent of 3-ethyl-3-oxetanemethanol, cationic photoinitiator of triaryl-sulfonium hexafluoroantimonate salts, and photosensitizer of PSS-303. Specimens were annealed at 350 °C for varying durations. Unannealed samples consisted of two phases, Te and a solid solution of Bi and Sb, while the annealed sample showed a single-phase of $\text{Bi}_{0.5}\text{Sb}_{1.5}\text{Te}_3$. Crystallinity increased with annealing duration. The density of all samples was less than that of a hot-pressed sample due to pore formation, amorphous carbon, and residual photoresins. Thermal conductivity was much lower than a hot-pressed sample with a minimum value of $0.2 \text{ W m}^{-1} \text{ K}^{-1}$ obtained for 50 wt % $\text{Bi}_{0.5}\text{Sb}_{1.5}\text{Te}_3$ at 44 °C, annealed for 1.5 h. Theoretical calculations confirm the temperature dependence of the lattice contribution of thermal conductivity for the 3D printed samples and the hot pressed sample are opposite, implying this fabrication method is promising for achieving a “phonon-glass” TE material. Higher $\text{Bi}_{0.5}\text{Sb}_{1.5}\text{Te}_3$ content yielded higher electrical conductivity which increases with prolonged annealing time, but was much lower than the hot-pressed sample. Seebeck coefficient was positive and higher for heavier $\text{Bi}_{0.5}\text{Sb}_{1.5}\text{Te}_3$ loading. The best ZT value was 0.12 at 43 °C, obtained with 60 wt % $\text{Bi}_{0.5}\text{Sb}_{1.5}\text{Te}_3$ annealed for 6 h.⁸³

CONCLUSION AND OUTLOOK

This review summarized four printing techniques used for fabrication of TE materials and devices and discussed their operating principles, advantages, and challenges relevant to TE materials. Results of recent work using these processes and materials were highlighted. The maximum powers achieved by the printed TE devices reviewed here cover a wide range from 54 pW to 50 μW , which is significantly lower than power generated by traditionally manufactured, inorganic TE devices that operate in the watt and kilowatt range. The field could benefit from standardized characterization techniques to enable meaningful comparison of materials, device geometries, and manufacturing methods. Although conversion efficiencies lag far behind those of their inorganic counterparts, organic and hybrid TE materials are significantly cheaper and suitable for printing manufacturing techniques

appropriate for large-scale production of thin and flexible TE devices. Such devices could power wearable electronics and enable low-grade waste heat recovery from non-planar surfaces.

REFERENCES

1. Zebarjadi, M.; Esfarjani, K.; Dresselhaus, M. S.; Ren, Z. F.; Chen, G. *Energ. Environ. Sci.* **2012**, *5*, 5147.
2. Estimated U.S. Energy Use in 2016. Lawrence Livermore National Laboratory, **2015**. Available at: <https://flowcharts.llnl.gov>. Last accessed January, 2016.
3. Jur, J. U.S. Pat. 0,311,421 A1 (**2015**).
4. Zhang, Q.; Sun, Y.; Xu, W.; Zhu, D. *Adv. Mater.* **2014**, *26*, 6829.
5. LeBlanc, S.; Yee, S. K.; Scullin, M. L.; Dames, C.; Goodson, K. E. *Renew. Sustain. Energ. Rev.* **2014**, *32*, 313.
6. alphabetenergy.com
7. LeBlanc, S. *Sustain. Mater. Technol.* **2014**, *1*, 26.
8. He, M.; Qiu, F.; Lin, Z. *Energ. Environ. Sci.* **2013**, *6*, 1352.
9. Heeger, A. J. *Synth. Met.* **2001**, *125*, 23.
10. Sun, K.; Zhang, S.; Li, P.; Xia, Y.; Zhang, X.; Du, D.; Isikgor, F. H.; Ouyang, J. *J. Mater. Sci. Mater. Electron.* **2015**, *26*, 4438.
11. Park, B. T.; Park, C.; Kim, B.; Shin, H.; Kim, E.; Park, T. *Energ. Environ. Sci.* **2013**, *6*, 788.
12. Kim, G. H.; Shao, L.; Zhang, K.; Pipe, K. P. *Nat. Mater.* **2013**, *12*, 719.
13. Weathers, A.; Khan, Z. U.; Brooke, R.; Evans, D.; Pettes, M. T.; Andreasen, J. W.; Crispin, X.; Shi, L. *Adv. Mater.* **2015**, *27*, 2101.
14. Nardes, A. M.; Kemerink, M.; Janssen, R. A. J.; Bastiaansen, J. A. M.; Kiggen, N. M. M.; Langeveld, B. M. W.; Van Breemen, A. J. J. M.; De Kok, M. M. *Adv. Mater.* **2007**, *19*, 1196.
15. Liu, J.; Wang, X.; Li, D.; Coates, N. E.; Segalman, R. A.; Cahill, D. G. *Macromolecules* **2015**, *48*, 585.
16. Wei, Q.; Mukaida, M.; Kirihara, K.; Ishida, T. *ACS Macro Lett.* **2014**, *3*, 948.
17. Wilson, P.; Lei, C.; Lekakou, C.; Watts, J. F. *Org. Electron.* **2014**, *15*, 2043.
18. Bubnova, O.; Khan, Z. U.; Malti, A.; Braun, S.; Fahlman, M.; Berggren, M.; Crispin, X. *Nat. Mater.* **2011**, *10*, 429.
19. Yu, C.; Choi, K.; Yin, L.; Grunlan, J. C. *ACS Nano* **2013**, *7*, 9506.
20. Nakai, Y.; Honda, K.; Yanagi, K. *Appl. Phys.* **2014**, *2*, 025103.
21. Nonoguchi, Y.; Ohashi, K.; Kanazawa, R.; Ashiba, K.; Hata, K.; Nakagawa, T.; Adachi, C.; Tanase, T.; Kawai, T. *Sci. Rep.* **2013**, *3*, 3344.
22. Suemori, K.; Hoshino, S.; Kamata, T. *Appl. Phys. Lett.* **2013**, *103*, 153902. Available at: <https://dx.doi.org/10.1063/1.4824648>.
23. Fukumaru, T.; Fujigaya, T.; Nakashima, N. *Sci. Rep.* **2015**, *5*, 7951.
24. Gao, C.; Chen, G. *Compos. Sci. Technol.* **2016**, *124*, 52.

25. Xu, K.; Chen, G.; Qiu, D. *J. Mater. Chem. A* **2013**, *1*, 12395.
26. Malen, J. A.; Yee, S. K.; Majumdar, A.; Segalman, R. A. *Chem. Phys. Lett.* **2010**, *491*, 109.
27. Ireland, R. M.; Katz, H. E. In *Innovative Thermoelectric Materials: Polymer, Nanostructure and Composite Thermoelectrics*; Katz, H. E.; Poehler, T. O., Eds.; Imperial College Press, **2016**.
28. Coates, N. E.; Yee, S. K.; McCulloch, B.; See, K. C.; Majumdar, A.; Segalman, R. A.; Urban, J. *J. Adv. Mater.* **2013**, *25*, 1629.
29. Urban, J. J.; Coates, N. E. In *Innovative Thermoelectric Materials: Polymer, Nanostructure, and Composite Thermoelectrics*; Katz, H. E.; Poehler, T. O., Eds.; Imperial College Press, Singapore, **2016**; p 107.
30. Yang, J.; Yip, H. L.; Jen, A. K. Y. *Adv. Energ. Mater.* **2013**, *3*, 549.
31. Lu, Z.; Layani, M.; Zhao, X.; Tan, L. P.; Sun, T.; Fan, S.; Yan, Q.; Magdassi, S.; Hng, H. H. *Small* **2014**, *10*, 3551.
32. Available at: <http://www.otego.de/en/#body>.
33. Available at: <https://globenewswire.com/news-release/2016/02/17/811378/0/en/PARC-Secures-ARPA-E-Funding-to-Demonstrate-How-Co-Extrusion-Printing-Technology-Can-be-Used-to-Make-Flexible-Large-Area-Thermoelectric-Generators-LATEGS.html>.
34. Basaran, O. A.; Gao, H.; Bhat, P. P. *Annu. Rev. Fluid Mech.* **2013**, *45*, 85.
35. Chen, A.; Madan, D.; Wright, P. K.; Evans, J. W. *J. Micro-mech. Microeng.* **2011**, *21*, 104006.
36. Knowlton, S.; Onal, S.; Yu, C. H.; Zhao, J. J.; Tasoglu, S. *Trends Biotechnol.* **2015**, *33*,
37. Cao, Z.; Koukharenko, E.; Tudor, M. J.; Torah, R. N.; Beeby, S. P. *Sensor. Actuat. A Phys.* **2016**, *238*, 196.
38. Jiao, F.; Di, C. -a.; Sun, Y.; Sheng, P.; Xu, W.; Zhu, D. *Philos. Trans. R. Soc. A Math. Phys. Eng. Sci.* **2014**, *372*, 20130008.
39. Søndergaard, R. R.; Hösel, M.; Espinosa, N.; Jørgensen, M.; Krebs, F. C. *Energ. Sci. Eng.* **2013**, *1*, 81.
40. Khan, S.; Lorenzelli, L.; Dahiya, R. S. *IEEE Sens. J.* **2015**, *15*, 3164.
41. Hoath, S. D. In *Fundamentals of Inkjet Printing*; Wiley-VCH: Weinheim, Germany, **2016**.
42. Wijshoff, H. *Phys. Rep.* **2010**, *491*, 77.
43. Martin, G. D.; Hoath, S. D.; Hutchings, I. M. *J. Phys. Conf. Ser.* **2008**, *105*, 012001.
44. Derby, B. *Annu. Rev. Mater. Res.* **2010**, *40*, 395.
45. Piqué, A.; Chrisey, D. B. In *Direct-Write Technologies for Rapid Prototyping Applications: Sensors, Electronics, and Integrated Power Sources*; Academic Press: San Diego, **2002**.
46. Hobby, A. *Circuit World* **1990**, *16*, 16.
47. Bártolo, P. In *Stereolithography: Materials, Processes, and Applications*; Springer: New York, **2011**.
48. Cao, Z.; Shi, J. J.; Torah, R. N.; Tudor, M. J.; Beeby, S. P. *J. Phys. Conf. Ser.* **2015**, *660*, 012096.
49. Besgan, A.; Zöllmer, V.; Kun, R.; Pál, E.; Walder, L.; Busse, M. *Procedia Technol.* **2014**, *15*, 99.
50. Drahi, E.; Gupta, A.; Blayac, S.; Saunier, S.; Benaben, P. *Phys. Status Solidi Appl. Mater. Sci.* **2014**, *211*, 1301.
51. Drahi, E.; Blayac, S.; Borbely, A.; Benaben, P. *Thin Solid Films* **2015**, *574*, 169.
52. Kamyshny, A.; Steinke, J.; Magdassi, S. *Open Appl. Phys. J.* **2011**, *4*, 19.
53. Li, D.; Sutton, D.; Burgess, A.; Graham, D.; Calvert, P. D. *J. Mater. Chem.* **2009**, *19*, 3719.
54. Walker, S. B.; Lewis, J. A. *J. Am. Chem. Soc.* **2012**, *134*, 1419.
55. Available at: <http://www.dupont.com/products-and-services/membranes-films/polyimide-films/brands/kapton-polyimide-film.html>
56. Jang, D.; Kim, D.; Moon, J. *Langmuir* **2009**, *25*, 2629.
57. Yu, W.; Xie, H. *J. Nanomater.* **2012**, *2012*, 1.
58. Haddad, Z.; Abid, C.; Oztog, H. F.; Mataoui, A. *Int. J. Therm. Sci.* **2014**, *76*, 168.
59. Li, Y.; Zhou, J.; Tung, S.; Schneider, E.; Xi, S. *Powder Technol.* **2009**, *196*, 89.
60. Wang, X. Ph. D. dissertation, School of Polymer, Textile and Fiber Engineering, Georgia Tech, Atlanta, GA, **2008**
61. Duffy, J. *Analytical Strategies for Ink Formulation*; Malvern Instruments, Malvern, United Kingdom, **2015**.
62. Deegan, R. D.; Bakajin, O.; Dupont, T. F.; Huber, G.; Nagel, S. R.; Witten, T. A. *Phys. Rev. E Stat. Physics, Plasmas, Fluids, Relat. Interdiscip. Top* **2000**, *62*, 756.
63. Eral, H. B.; Augustine, D. M.; Duits, M. H. G.; Mugele, F. *Soft Matter* **2011**, *7*, 4954.
64. Lim, J. A.; Lee, W. H.; Lee, H. S.; Lee, J. H.; Park, Y. D.; Cho, K. *Adv. Funct. Mater.* **2008**, *18*, 229.
65. Shimoni, A.; Azoubel, S.; Magdassi, S. *Nanoscale* **2014**, *6*, 1.
66. Still, T.; Yunker, P. J.; Yodh, A. G. *Langmuir* **2012**, *28*, 4984.
67. Anyfantakis, M.; Geng, Z.; Morel, M.; Rudiuk, S.; Baigl, D. *Langmuir* **2015**, *31*, 4113.
68. Menon, A. K.; Yee, S. K. *J. Appl. Phys.* **2016**, *119*, 055501.
69. Sun, Y.; Sheng, P.; Di, C.; Jiao, F.; Xu, W.; Qiu, D.; Zhu, D. *Adv. Mater.* **2012**, *24*, 932.
70. Niittynen, J.; Abbel, R.; Mäntysalo, M.; Perelaer, J.; Schubert, U. S.; Lupo, D. *Thin Solid Films* **2014**, *556*, 452.
71. Oghbaei, M.; Mirzaee, O. *J. Alloys Compd.* **2010**, *494*, 175.
72. McSweeney, T. B. In *Coatings Technology: Fundamentals, Testing, and Processing Techniques*; Tracton, A., Eds.; CRC Press: Boca Raton, **2007**, 24-1.
73. Rudež, R.; Markowski, P.; Presečnik, M.; Košir, M.; Dziedzic, A.; Bernik, S. *Ceram. Int.* **2015**, *41*, 13201.
74. Kim, S. J.; We, J. H.; Kim, J. S.; Kim, G. S.; Cho, B. J. *J. Alloys Compd.* **2014**, *582*, 177.
75. Kim, S. J.; We, J. H.; Cho, B. J. *Energ. Environ. Sci.* **2014**, *7*, 1959.
76. We, J. H.; Kim, S. J.; Kim, G. S.; Cho, B. J. *J. Alloys Compd.* **2013**, *552*, 107.
77. Wei, Q.; Mukaida, M.; Kirihara, K.; Naitoh, Y.; Ishida, T. *RSC Adv.* **2014**, *4*, 28802.

78. Krebs, F. C.; Jørgensen, M.; Norrman, K.; Hagemann, O.; Alstrup, J.; Nielsen, T. D.; Fyenbo, J.; Larsen, K.; Kristensen, J. *Sol. Energ. Mater. Sol. Cells* **2009**, *93*, 422.
79. Rudež, R.; Pavlič, J.; Bernik, S. *J. Eur. Ceram. Soc.* **2015**, *35*, 3013.
80. Lewis, J. A. *Adv. Funct. Mater.* **2006**, *16*, 2193.
81. Vaezi, M.; Seitz, H.; Yang, S. *Int. J. Adv. Manuf. Technol.* **2013**, *67*, 1721.
82. Chen, A.; Madan, D.; Koplów, M.; Wright, P. K.; Evans, J. W. *Proc. PowerMEMS* **2009**, 2009, 277.
83. He, M.; Zhao, Y.; Wang, B.; Xi, Q.; Zhou, J.; Liang, Z. *Small* **2015**, *11*, 5889.
84. Wong, K. V.; Hernandez, A. *ISRN Mech. Eng.* **2012**, 2012, 1.
85. Halloran, J. W.; Tomeckova, V.; Gentry, S.; Das, S.; Cilino, P.; Yuan, D.; Guo, R.; Rudraraju, A.; Shao, P.; Wu, T.; Alabi, T. R.; Baker, W.; Legdzina, D.; Wolski, D.; Zimbeck, W. R.; Long, D. *J. Eur. Ceram. Soc.* **2011**, *31*, 2613.
86. Maruo, S.; Kawata, S. *J. Microelectromech. Syst.* **1998**, *7*, 411.
87. Park, S. H.; Lim, T. W.; Yang, D. Y.; Cho, N. C.; Lee, K. S. *Appl. Phys. Lett.* **2006**, *89*, 173133.
88. Pham, D. T.; Ji, C. *Proc. Inst. Mech. Eng. Part C J. Mech. Eng. Sci.* **2000**, *214*, 635.
89. Wicker, R. B.; MacDonald, E. W. *Virtual Phys. Prototype* **2012**, *7*, 181.
90. Sager, B.; Rosen, D. W.; Shilling, M.; Kurfess, T. R. Presented at the International Solid Freeform Fabrication Symposium, Austin, TX, **2003**; p 70.